Research Article | Vol. 26, No. 18 | 3 Sep 2018 | OPTICS EXPRESS 23380
Optics EXPRESS

Detection of periodic structures through opaque metal layers by optical measurements of ultrafast electron dynamics

S. EDWARD,[1,2,*] A. ANTONCECCHI,[1,3] H. ZHANG,[1] H. SIELCKEN,[4] S. WITTE,[1,3] AND P. C. M. PLANKEN[1,2]

[1]*Advanced Research Center for Nanolithography (ARCNL), Science Park 110, 1098 XG Amsterdam, The Netherlands*
[2]*Van der Waals-Zeeman Institute, University of Amsterdam, Science Park 904, 1098 XH Amsterdam, The Netherlands*
[3]*Department of Physics and Astronomy, Vrije Universiteit, De Boelelaan 1081, 1081 HV Amsterdam, The Netherlands*
[4]*AMOLF, Science Park 104, 1098 XH Amsterdam, The Netherlands*
[*]*sedward@arcnl.nl*

Abstract: We report on femtosecond optical pump-probe measurements of ultrafast electron dynamics to detect the presence of gratings buried underneath optically opaque gold layers. Electron energy diffusion and cooling are found to be strongly affected by the presence and type of metal buried below the gold layer. As a result, the spatially periodic buried grating is encoded on the electron temperature near the top surface, leading to a spatially periodic modulation of the optical properties near the gold surface from which a delayed probe pulse can be diffracted. Our measurements show that these effects may be useful for optical detection and alignment applications in semiconductor device manufacturing.

OCIS codes: (310.6860) Thin films, optical properties; (160.3900) Metals; (120.3940) Metrology; (320.7100) Ultrafast measurements.

References and links

1. T. Avanesian and P. Christopher, "Adsorbate specificity in hot electron driven photochemistry on catalytic metal surfaces," J. Phys. Chem. C **118**, 28017–28031 (2014).
2. J. W. Gadzuk, "Hot-electron femtochemistry at surfaces: on the role of multiple electron processes in desorption," Chem. Phys. **251**, 87–97 (2000).
3. O. Matsuda, M. C. Larciprete , R. L. Voti, and O. B. Wright, "Fundamentals of picosecond laser ultrasonics," Ultrasonics **56**, 3–20 (2015).
4. P. Ruello, and V. E. Gusev, "Physical mechanisms of coherent acoustic phonons generation by ultrafast laser action," Ultrasonics **56**, 21–35 (2015).
5. P. B. Corkum, F. Brunel, N. K. Sherman, and T. Srinivasan-Rao, "Thermal response of metals to ultrashort-pulse laser excitation," Phys. Rev. Lett. **61**, 2886–2889 (1988).
6. G. K. P. Ramanandan, G. Ramakrishnan, N. Kumar, A. J. L. Adam, and P. C. M. Planken, "Emission of terahertz pulses from nanostructured metal surfaces," J. Phys. D: Appl. Phys. **47**, 374003 (2014).
7. G. Ramakrishnan and P. C. M. Planken, "Percolation-enhanced generation of terahertz pulses by optical rectification on ultrathin gold films," Opt. Lett. **36**, 2572–2574 (2011).
8. F. Kadlec, P. Kužel, and J. -L. Coutaz, "Optical rectification at metal surfaces," Opt. Lett. **29**, 2674–2676 (2004).
9. F. Kadlec, P. Kužel, and J. -L Coutaz, "Study of terahertz radiation generated by optical rectification on thin gold films," Opt. Lett. **30**, 1402–1404 (2005).
10. J. Hohlfeld, S.-S. Wellershoff, J. Güdde, U. Conrad, V. Jähnke, and E. Matthias, "Electron and lattice dynamics following optical excitation of metals," Chem. Phys. **251**, 237–258 (2000).
11. W. S. Fann, R. Storz, H. W. K. Tom, and J. Bokor, "Direct measurement of nonequilibrium electron-energy distributions in subpicosecond laser-heated gold films," Phys. Rev. Lett. **68**, 2834–2837 (1992).
12. W. S. Fann, R. Storz, H. W. K. Tom, and J. Bokor, "Electron thermalization in gold," Phys. Rev. B **46**, 13592–13595 (1992).
13. C. Suarez, W. E. Bron, and T. Juhasz, "Dynamics and transport of electronic carriers in thin gold films," Phys. Rev. Lett. **75**, 4536–4539 (1995).

#327654 https://doi.org/10.1364/OE.26.023380
Journal © 2018 Received 6 Apr 2018; revised 26 Jul 2018; accepted 30 Jul 2018; published 28 Aug 2018

Optics EXPRESS

14. J. Hohlfeld, J.G. Müller, S.-S. Wellershoff, and E. Matthias, "Time-resolved thermoreflectivity of thin gold films and its dependence on film thickness," Appl. Phys. B **64**, 387–390 (1997).
15. J. Hohlfeld, D. Grosenick, U. Conrad, and E. Matthias, "Femtosecond time-resolved reflection second-harmonic generation on polycrystalline copper," Appl. Phys. A **60**, 137–142 (1995).
16. M. Bonn, D. N. Denzler, S. Funk, M. Wolf, S. -Svante Wellershoff and Julius Hohlfeld, "Ultrafast electron dynamics at metal surfaces: Competition between electron-phonon coupling and hot-electron transport," Phys. Rev. B **61**, 1101–1105 (2000).
17. S. D. Brorson, A. Kazeroonian, J. S. Moodera, D. W. Face, T. K. Cheng, E. P. Ippen, M. S. Dresselhaus, and G. Dresselhaus, "Femtosecond room-temperature measurement of the electron-phonon coupling constant γ in metallic superconductors," Phys. Rev. Lett. **64**, 2172–2175 (1990).
18. J. L. Hostetler, A. N. Smith, D. M. Czajkowsky, and P. M. Norris, "Measurement of the electron-phonon coupling factor dependence on film thickness and grain size in Au, Cr, and Al," Applied Optics **38**, 3614–3620 (1999).
19. P. E. Hopkins, and P. M. Norris, "Substrate influence in electron–phonon coupling measurements in thin Au films," Applied Surface Science **253**, 6289–6294 (2007).
20. T. Juhasz, H. E. Elsayed-Ali, G. O. Smith, C. Suarez, and W. E. Bron, "Direct measurements of the transport of nonequilibrium electrons in gold films with different crystal structures," Phys. Rev. B **48**, 15488–15491(R) (1993).
21. T. Q. Qiu and C. L. Tien, "Short-pulse laser heating on metals," Int. J. Heat Mass Transfer **35**, 719–726 (1992).
22. A. N. Smith, and P. M. Norris, "Influence of intraband transitions on the electron thermoreflectance response of metals," Appl. Phys. lett. **78**, 1240–1242 (2001).
23. P. E. Hopkins, J. L. Kassebaum, and P. M. Norris, "Effects of electron scattering at metal-nonmetal interfaces on electron-phonon equilibration in gold films," J. Appl. Phys. **105**, 023710 (2009).
24. T. Juhasz, H. E. Elsayed-Ali, X. H. Hu, and W. E. Bron, "Time-resolved thermoreflectivity of thin gold films and its dependence on the ambient temperature," Phys. Rev. B **45**, 13819–13822(R) (1992).
25. R. H. M. Groeneveld, R. Sprik, and A. Lagendijk, "Effect of a nonthermal electron distribution on the electron-phonon energy relaxation process in noble metals," Phys. Rev. B **45**, 5079–5082(R) (1992).
26. W. M. G. Ibrahim, H. E. Elsayed-Ali, C. E. Bonner Jr., and M. Shinn, "Ultrafast investigation of electron dynamics in multi-layer metals," Int. J. Heat Mass Transfer **47**, 2261–2268 (2004).
27. A. Chen, L. Sui, Y. Shi, Y. Jiang, D. Yang, H. Liu, M. Jin, and D. Ding, "Ultrafast investigation of electron dynamics in the gold-coated two-layer metal film," Thin Solid Films **529**, 209–216 (2013).
28. J. Guo, T. Wang, D. Wang, J. Shao, A. Chen, and M. Jin, "Simulation of thermionic emission optimization in femtosecond laser irradiation metal film by two-layer structure," Appl. Phys. A **117**, 1367–1374 (2014).
29. S. D. Brorson, J. G. Fujimoto, and E. P. Ippen, "Femtosecond electronic heat-transport dynamics in thin gold films," Phys. Rev. Lett. **59**, 1962–1965 (1987).
30. M. Aeschlimann, M. Bauer, S. Pawlik, W. Weber, R. Burgermeister, D. Oberli, and H. C. Siegmann, "Ultrafast spin-dependent electron dynamics in fcc Co," Phys. Rev. Lett. **79**, 5158–5161 (1997).
31. C. -K. Sun, F. Vallée, L. H. Acioli, E. P. Ippen, and J. G. Fujimoto, "Femtosecond-tunable measurement of electron thermalization in gold," Phys. Rev. B **50**, 15337–15348 (1994).
32. C.-K. Sun, F. Vallée, L. H. Acioli, E. P. Ippen, and J. G. Fujimoto, "Femtosecond investigation of electron thermalization in gold," Phys. Rev. B **48**, 12365–12368 (1993).
33. T. F. Crimmins, A. A. Maznev, and K. A. Nelson, "Transient grating measurements of picosecond acoustic pulses in metal film," Appl. Phys. Lett. **74**, 1344–1346 (1999).
34. A. M. Chen, Y. F. Jiang, L. Z. Sui, H. Liu, M. X. Jin and D. J. Ding, "Thermal analysis of double-layer metal films during femtosecond laser heating," J.Opt. **13**, 055503 (2011).
35. W. Wang and D. G. Cahill, "Limits to thermal transport in nanoscale metal bilayers due to weak electron-phonon coupling in Au and Cu," Phys. Rev. Lett. **109**, 175503 (2012).
36. G. D. Tsibidis, "Thermal response of double-layered metal films after ultrashort pulsed laser irradiation: The role of nonthermal electron dynamics," Appl. Phys. Lett. **104**, 051603 (2014).
37. G. -M. Choi, R. B. Wilson, and D. G. Cahill, "Indirect heating of Pt by short-pulse laser irradiation of Au in a nanoscale Pt/Au bilayer," Phys. Rev. B **89**, 064307 (2014).
38. A. M. Chen, H. F. Xu, Y. F. Jiang, L. Z. Sui, D. J. Ding, H. Liu, and M .X. Jin, "Modeling of femtosecond laser damage threshold on the two-layer metal films," Appl. Surf. Sci. **257**, 1678–1683 (2010).
39. A. Guerra III, W. E. Bron, and C. Suárez, "Imaging metallic multilayer structures through ultrafast optically driven excited electron transport," Appl. Phys. B **68**, 405–409 (1999).
40. A. J. den Boef, "Optical wafer metrology sensors for process-robust CD and overlay control in semiconductor device manufacturing," Surf. Topogr. Metrol. Prop. **4**, 023001 (2016).
41. H. J. Eichler, P. Günter, and D. W. Pohl, *Laser-induced dynamic gratings*, (Springer, 1986).
42. M. Perner, P. Bost, U. Lemmer, G. von Plessen, J. Feldmann, U. Becker, M. Mennig, M. Schmitt, and H. Schmidt, "Optically induced damping of the surface plasmon resonance in gold colloids," Phys. Rev. Lett. **78**, 2192–2195 (1997).
43. M. Lejman, V. Shalagatskyi, O. Kovalenko, T. Pezeril, V. V. Temnov, and P. Ruello, "Ultrafast optical detection of coherent acoustic phonons emission driven by superdiffusive hot electrons," J. Opt. Soc. Am. B **31**, 282–290 (2014) .
44. T. Dehoux, N. Chigarev, C. Rossignol, and B. Audoin, "Effect of lateral electronic diffusion on acoustic diffraction in picosecond ultrasonics," Phys. Rev. B **77**, 214307 (2008).

Optics EXPRESS

45. S. I. Anisimov, B. L. Kapeliovich, and T. L. Perel'man, "Electron emission from metal surfaces exposed to ultrashort laser pulses," Zh. Eksp. Teor. Fiz. **66**, 776–781 (1974)(Sov. Phys. JETP 39, 375-377 (1974)).
46. H. E. Elsayed-Ali, T. B. Norris, M. A. Pessot, and G. A. Mourou, "Time-resolved observation of electron-phonon relaxation in copper," Phys. Rev. Lett. **58**, 1212–1215 (1987).
47. Z. Lin, L. V. Zhigilei, and V. Celli, "Electron-phonon coupling and electron heat capacity of metals under conditions of strong electron-phonon nonequilibrium," Phys. Rev. B **77**, 075133 (2008).
48. P. B. Johnson and R. W. Christy, "Optical constants of the noble metals," Phys. Rev. B **6**, 4370–4379 (1972).

1. Introduction

The interaction of femtosecond laser pulses with metals has been an area of active research in photochemistry [1, 2], laser-induced ultrasonics [3, 4], laser ablation [5], and in the generation of coherent terahertz pulses from the surface of metals [6–9]. Numerous studies have led to an improved understanding of the fundamental processes involved when a femtosecond laser pulse irradiates metal layers of nanometer-scale thickness [10–28]. When a femtosecond pulse is absorbed by the metal within the optical skin depth, a non-thermal distribution of excited electrons is created. These electrons undergo ballistic and diffusive motion and thermalize to a Fermi-Dirac distribution, due to electron-electron scattering, on a time scale of up to hundreds of femtoseconds [29–33]. This thermalized electron gas cools by heating up the lattice, a process that typically takes a few picoseconds.

Surprisingly, although electron dynamics following ultrafast optical excitation in single metal layers of nanometer-scale thickness is fairly well understood, only a few experimental studies of metallic *bilayers* have been published. The presence of one type of metal below a layer made of a different metal is not only expected to affect the electron dynamics in the top layer [26–28, 34–36], but also the location inside the bilayer system where lattice heating occurs [37, 38]. This is obviously highly relevant for ablation experiments, but, interestingly enough, they also hint at the possibility to use these effects to detect and, possibly, image buried metal layers and buried micro-and nano-structures [39]. For example, in semiconductor device manufacturing it is often necessary to detect the presence and exact position of one metal, for instance in the shape of a line or a grating, buried underneath a different metal [40]. If the top metal is optically opaque, standard optical techniques can no longer be used, but optically measuring the effect that the bottom metal has on the electron dynamics near the surface of the top metal may be a viable alternative.

Here, we show that gold and copper gratings, buried below an optically opaque, flat gold layer, can be detected at the surface of the gold by observing transient optical diffraction. The transient diffraction is the result of an electron temperature grating that forms after exciting the flat gold layer with a single femtosecond laser pulse. This temperature grating is the result of the different electron dynamics above the valleys and the trenches of the real, buried grating and leads to a grating in the optical constants near the surface of the gold from which a probe pulse can be diffracted. Time resolved diffraction measurements on *flat* metallic bilayers, in which two overlapping and interfering pump pulses form a spatially periodic, grating-like excitation pattern, confirm that electron dynamics is a sensitive probe of the type and thickness of the buried metal underneath the opaque gold layer. They hint at the possibility to use these effects for optical detection and alignment applications.

2. Experimental setup

A schematic of the experimental setup used for our experiments is shown in Fig. 1. The laser system used is a Ti:Sapphire multi-pass amplifier (Femtopower, Spectra Physics) generating 30 fs pulses, with a wavelength centered at 800 nm and with a repetition rate of 1 kHz. The output from the laser is split into two using a 1% beam splitter. The stronger part is frequency doubled with a 100 μm BBO crystal to generate 400 nm pump pulses. A half wave plate (HWP)

Optics EXPRESS

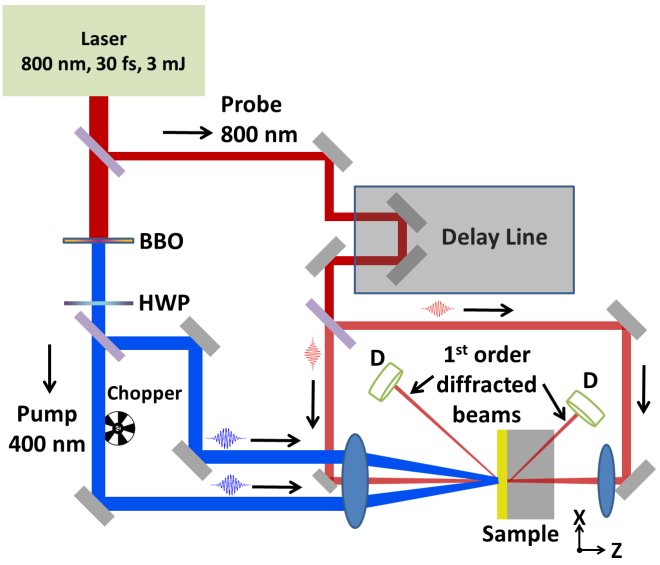

Fig. 1. Schematic of the experimental setup: components include a non-linear optical crystal (BBO), Half Wave Plate (HWP) and a Photodiode (D). The two frequency-doubled 400 nm pump pulses are focused onto the sample at the same position, but under different angles to form a spatially periodic intensity pattern. The 800 nm probe pulse that diffracts off the resulting grating in the optical constants of the sample, is recorded by the detectors while the delay line is used to change the pump-probe delay.

rotates the polarization of the 400 nm pump pulse by 90^o so that both the pump and the probe are p-polarized. For experiments on flat samples, the pump pulses are split into two by a 50% beamsplitter. One part passes through a 500 Hz mechanical chopper. Both beams are then weakly focused onto the sample at a different angle. On the sample, the two pump pulses overlap in space and time to create a spatially periodic interference pattern with a period determined by the angle between the beams. In our experiments, we have a grating period of 6 μm. The spatially periodic excitation of the metal leads to spatially periodic changes in the optical constants of the metal, that can be observed by diffracting a delayed probe pulse off the transient grating. By measuring the diffracted signal as a function of the pump-probe delay, we can measure the decay of this transient grating, giving information on the electron dynamics. Using different wavelengths for pump and probe allows us to use optical filters to block scattered pump light from entering the probe detector. The diffracted pulse energy is recorded by a silicon photodiode placed at the position where we expect the first-order diffracted beam. The analog signal recorded from the photodiode is converted to a digital signal and averaged over 100 pulses. The diffracted probe signal recorded by the detector when the chopper blocks the pump beam is subtracted from the diffracted probe signal when the pump beam is transmitted by the chopper and plotted as a function of the pump-probe delay. The signal recorded by the detector in the absence of the pump pulse is from probe light scattered by the surface roughness of the sample. Depending on the experiment, we probe from the front surface or from the back surface. In the latter case, the probe pulse passes through the glass substrate and probes the metal near the glass-metal interface. The pump beam has a spot size of 1.5 mm on the sample and the pump pulse energy ranges from 3 μJ to 15 μJ depending on the experiment. The probe pulse energy was kept constant at 1 μJ. This is a significant fraction of the pump-pulse energy to maximize the possibility of detecting signals on samples demonstrating a low diffraction efficiency. However, in our experiments we mostly pump and probe Au in which about 60% of the 400 nm wavelength pump-pulse energy is

Optics EXPRESS

absorbed and only about 2% of the 800 nm wavelength probe-pulse energy. No two-photon probe absorption was observed within the measurement accuracy of our setup. The typical diffraction efficiencies, recorded when the pump and probe overlap, range from 10^{-5} to 10^{-4}, depending on the pump pulse energy and the sample thickness. For the experiments on the physically buried metal grating, only *one* pump beam is used.

All samples used in the experiments are prepared by physical vapor deposition at a pressure below 10^{-6} mbar on a chemically cleaned glass substrate. The film thickness was determined using a quartz crystal thickness monitor with a ± 5% uncertainty. For experiments on bilayer thin films, the materials were evaporated one after the other without disturbing the vacuum of the evaporator. The metal gratings on the flat layer of gold were fabricated by UV lithography.

3. Numerical calculations

For a proper understanding of our experiments on flat bilayer samples and buried grating samples, it is important to calculate where the optical energy is deposited inside the material. To calculate this, we solve Maxwell's equations for an electromagnetic field in four different materials and multiply the result with a Gaussian envelope in time, which corresponds to the temporal profile of the pulse. This resembles the experiment in which, air, the first metal, the second metal and the substrate are the four different materials through which the laser pulse propagates. It is important to calculate the intensity of the light directly hitting the second metal layer because this will also affect the electron-lattice dynamics at the surface of the first metal layer. More information on this can be found in Appendix A.

To gain some insight into the physical processes taking place during and after optical excitation, we also performed calculations of the electron and lattice temperatures using the well-known two-temperature model (TTM) (see Appendix B). As we will show in the following sections, we find a remarkable correspondence between the measured, time-dependent, diffracted signal, and the calculated time-dependent electron temperature. There is no a priori reason to assume that the diffraction efficiency η should linearly depend on the change in the electron temperature ΔT_e. It can be shown that the diffraction efficiency η scales as $\eta \propto (\Delta\epsilon)^2$, with $\Delta\epsilon$ being the change in the complex dielectric function [41]. If we assuming that changes in the dielectric function are dominated by changes in the electron gas temperature ΔT_e, we conclude that this linear relation must imply $\Delta\epsilon \propto \sqrt{\Delta T_e}$. This is different from the often made assumption that $\Delta\epsilon \propto \Delta T_e$ [23,27,32] or $\Delta\epsilon \propto \Delta(T_e)^2$ [25,42]. We currently do not know what the origin is of the different temperature dependencies of the dielectric function extracted from the experiments. A full theoretical analysis of the time-dependent complex dielectric function after optical excitation requires detailed calculations of the contribution of inter- and intraband transitions to the changes in the complex dielectric function. Hohlfeld et. al. [15] showed that this can give satisfactory results, but such an effort is beyond the scope of this paper. Here, we focus on the ability to use electron dynamics to detect gratings, buried below an opaque metal. It is interesting, though, that our calculations of the electron temperature use only material parameters known from the literature. Only the electron-phonon coupling constant of gold that we use is on the low side of the range of values found in the literature. There are no adjustable parameters in our model as excitation parameters are taken from the experimental values. We have placed calculations of the time-dependent electron temperature alongside some of the measurements as they provide important physical insight into the electron and lattice dynamics occurring after excitation.

4. Results and discussion

Prior to our experiments on buried gratings, we performed pump-probe experiments with interfering pump pulses forming a spatially periodic, grating-like excitation pattern, on single layers of gold (section 4.1) and gold-metal bilayers (section 4.2 and 4.3). This was done to obtain

Optics EXPRESS

a better understanding of the electron dynamics and, in a few cases, to compare with results known from literature.

4.1. Electron dynamics in gold

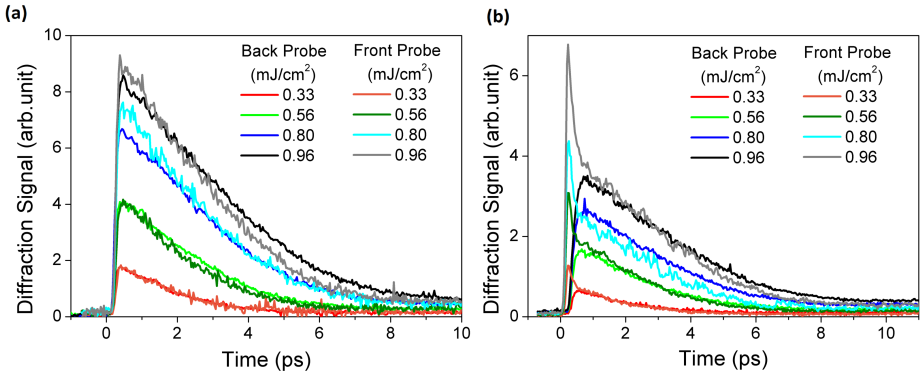

Fig. 2. Diffracted front-probe and back-probe signal as a function of pump-probe delay at various pump fluences for (a) 45 nm gold layer and (b) 100 nm gold layer. The samples were pumped from the air-gold side and probed from the air-Au side (front probe) and the glass-Au side (back probe).

In Fig. 2, we plot the probe signal diffracted from both the air-Au interface (front) and the glass-Au interface (back), for two different thicknesses of Au, 45 nm in Fig. 2(a) and 100 nm in Fig. 2(b), for various pump powers. Additional measurements of the front probe diffraction efficiency as a function of time, for various thicknesses of gold are similar to those shown by others [14] and can be found in Appendix C. In all cases, the 400 nm pump beams illuminate the Au from the front-side. As it is difficult to compare the absolute diffraction efficiencies for the front and back-probe cases, we applied a scaling factor to the back-probe signal such, that for a single pump intensity, both the front-probe signal and the back-probe signal overlap as much as possible for time delays larger than 0.5 ps. We then use the *same* scaling factor for the curves at different intensities. Different scaling factors were used for the 45 nm Au and 100 nm Au back probe signals and the signal strengths shown in Fig. 2(a) cannot be compared with those in Fig. 2(b). In both figures, the front probe diffraction efficiency is seen to rise on a rapid time scale of $\approx$ 100 fs. For the 45 nm sample in Fig. 2(a), this then gradually decays towards zero for increasing time delays. For the 100 nm sample in Fig. 2(b), the decay is initially rapid, and then slows down. In both measurements, excitation with two spatially and temporally overlapping pump pulses results in a spatially periodic electron gas temperature $T_e(x,t)$ along the surface, in a direction perpendicular to the grating lines. This temperature grating is formed when in the bright fringes of the interference pattern the electron gas is rapidly heated whereas in the dark fringes, where the electron gas is not excited, the temperature remains 297 K. The amplitude of this electron-gas temperature grating, $\Delta T_e(t)$, is thus determined by the difference between the temperatures in the bright and the dark fringes. Heating of the electron gas leads to changes in the complex dielectric function of the metal. A grating in the electron-gas temperature thus leads to a grating in the dielectric function. From this grating, a probe pulse can be diffracted. As such, the diffracted signals observed in Fig. 2 are correlated with the dynamics of $\Delta T_e(t)$.

The rapid decay, observed during the first 0.5 ps for the 100 nm thick sample, was not observed by Hohlfeld et. al. [14], presumably because they used longer pulses in their experiments which

Optics EXPRESS

may have given rise to a smearing out of the sharp peak. Interestingly, the results show that for the 45 nm gold film the signal shapes for the front and back-probe signals are very similar. This observation agrees with the assumption that for thin layers, after optical excitation, the electron energy is quickly redistributed relatively homogeneously throughout the layer [14]. This redistribution causes the measured dynamics, now dominated by electron cooling through lattice heating, to be the same everywhere. However, for the 100 nm gold layer, the front- and back-probe signals are different. There, we find that the front probe signal shows a rapid rise and decay, but that the back-probe signal rises more slowly. For pump-probe time delays larger than about 0.5 ps, the signals look similar and, again only one vertical scaling factor is applied to the back-probe signals to overlap all the front- and back-probe signals for this sample. The sharp rise/fall time of the front-probe signal and the slower rise of the back-probe signal are the result of ballistic transport and diffusion of electron energy out of the front-surface front-probe interaction region towards and into the back-probe interaction region near the Au/glass interface [14]. For 100 nm Au this process takes a few hundred femtoseconds which explains the slower rise of the back-probe diffracted signal. This also means that after this time the electron energy distribution should be relatively homogeneous again, explaining why for delays larger than about 0.5 ps the front-and back-probe signals look similar.

4.2. *Electron dynamics in gold-platinum bilayers*

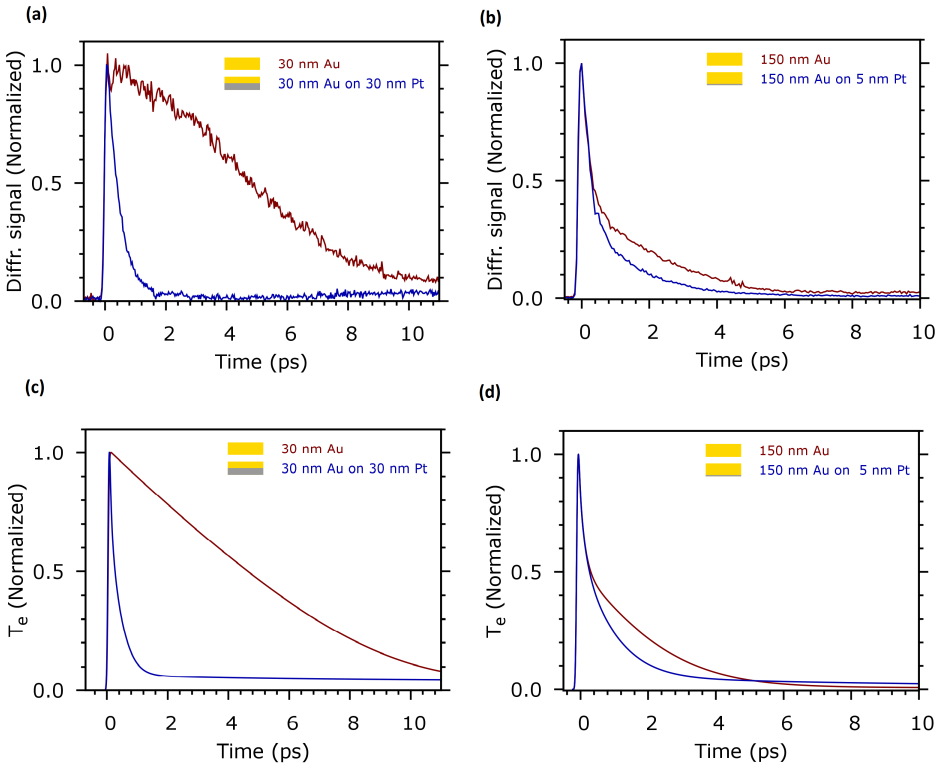

Fig. 3. (a) The measured front-probe diffracted signal vs. pump-probe delay for a pump fluence of 0.80 mJ/cm^2 on a sample with 30 nm Pt under 30 nm Au. (b) The experimentally measured front-probe diffracted signal vs. pump-probe delay on a sample with 5 nm Pt under 150 nm Au. (c) The numerically calculated electron temperature T_e vs. time for the sample with 30 nm Pt under 30 nm Au. (d) The numerically calculated T_e vs. time for the sample with 5 nm Pt under 150 nm Au.

Optics EXPRESS

To better understand the measurements on buried gratings discussed later in this paper, we also studied the effect that a buried metal layer has on the electron dynamics observed at the gold surface. Initially, we chose platinum as the buried metal layer due to its very high electron-phonon coupling strength when compared to gold. In Fig. 3(a) we plot the measured diffracted front-probe diffraction efficiency versus pump-probe time delay for a bilayer consisting of 30 nm of Au deposited on 30 nm of Pt. In the same figure, we also plot the time-dependent front-probe diffraction efficiency for a single 30 nm thick layer of Au. The figure shows that the presence of the Pt layer underneath the gold dramatically accelerates the decay of the diffracted probe signal. Note that, although no signal for a Au thickness of 60 nm was measured, the results shown in Fig. 2 for 45 and 100 nm thick single Au layers suggest that for 60 nm of gold, the decay would be in between these two cases and would still be significantly slower than for 30 nm of Au on Pt. To determine the limits of the effect that Pt has on the decay of the measured diffracted signal, we plot in Fig. 3(b) the front-probe diffraction efficiency versus pump-probe delay for a sample consisting of 150 nm of Au on 5 nm of Pt and for a sample consisting of 150 nm Au only. This gold layer thickness was chosen to eliminate the possibility of the 400 nm pump beam directly exciting the Pt since the 400 nm light has a penetration depth of about 16 nm in Au. Remarkably, the results show that for this particular bilayer, even the effect of a buried Pt layer as thin as 5 nm on the shape of the diffracted signal versus pump-probe delay, is still measurable. The tell-tale sign of the effect of the buried Pt layer is that the transition from an initial fast decay to a slower decay, as observed in the gold-only sample, is absent. This means that the difference between the single Au layer and the bilayer manifests itself most strongly for longer time delays, as shown in Fig. 3(b).

This difference in decay due to the presence of a platinum layer can be simulated using TTM calculations. In Fig. 3(c) and Fig. 3(d), we plot the calculated electron temperature at a depth of 8 nm from the top surface of the gold layer as a function of time, using the same parameters as in the experiments. For the sample with 30 nm Au on top of 30 nm Pt, the electron temperature decreases rapidly due to the presence of the platinum layer. For the sample with 5 nm Pt under 150 nm Au, the electron temperature decreases at a slightly slower rate than in 150 nm Au. We note that the calculation of the time-dependent electron temperature closely resembles the measurements of the diffraction efficiency versus pump-probe time delay.

We can explain this behavior by looking at the electron-lattice dynamics occurring in the buried platinum layer. After optical excitation, the electron energy diffuses deeper into the gold layer and beyond into the platinum layer. The electron-phonon coupling constant of platinum, however, is about two orders of magnitude higher than that of gold. This means that thermalized electrons that diffuse into the platinum, immediately lose energy to the Pt lattice and quickly cool. Thus, a strong electron-temperature gradient between the gold and platinum layer is maintained, which in turn drives the rate of electron gas energy diffusion out of the probe interaction region near the surface of gold into the deeper regions of the gold and into the platinum layer. These results are interesting, because they show that even a Pt layer as thin as 5 nm has a measurable effect on the decay observed near the surface of a 150 nm thick Au layer. This suggests that a pump-probe technique may be used for sub-surface metrology, in particular the localization and inspection of buried structures underneath optically opaque metal layers.

To confirm that the energy is deposited in the Pt layer, we performed experiments on a sample with 30 nm platinum on 30 nm gold in which we pump from the gold side and probe from the platinum side (back probe) as well as the gold side (front probe). In Fig. 4, we plot the diffracted front-probe and back-probe signal as a function of the pump-probe delay. As it is difficult to compare the absolute diffraction efficiencies for the front and back-probe cases, we instead applied a scaling factor to the back-probe signal so that both the front-probe signal and the back-probe signal can be plotted in the same graph. The back probe signal was smoothed by nearest neighbor averaging. For the front probe, the signal rises rapidly and then decays in

Optics EXPRESS

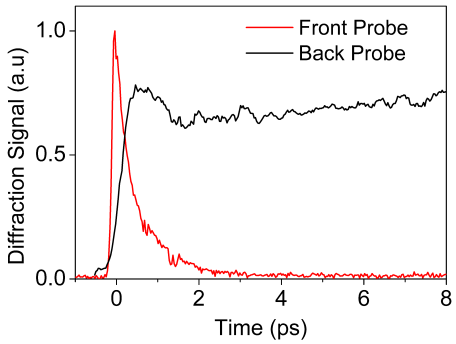

Fig. 4. The measured diffracted signal from the front-probe (red) and back-probe (black) for a pump fluence of 0.80 mJ/cm^2 on a sample with 30 nm Pt under 30 nm Au.

1-2 ps, indicating a rapid drop in electron temperature. This plot is similar to Fig. 3(a) and the physics has been discussed earlier in this section. In contrast, the signal from the back probe shows a gradual increase for about 0.7 ps followed by a small decrease to a lower value and then continues to increase very slightly.

This different behavior of the back probe signal vs. pump-probe time delay can be explained by including the lattice dynamics of the Pt-Au layer. The initial rise of the back-probe signal seen in Fig. 4 is interpreted as resulting from the diffusion of electron energy into the Pt layer and simultaneous heating of the Pt lattice by the electron gas. The small decay is the result of the cooling of the electron gas, but it is superimposed on the growing signal caused by the heating of the lattice. The slow and weak increase of the signal after 2 ps is real. The TTM calculations (not shown here) indicate that, at a time delay of about 1 ps, the Pt lattice temperature has a strong gradient, being higher near the Pt/Au interface and lower near the back of the Pt, where the probe pulse interacts with the Pt. Equilibration of the difference occurs through electron energy diffusion, where electrons pick up the lattice energy from the hotter regions, and deposit this in the cooler regions. The latter gives rise to a slowly increasing lattice temperature in the regions where the probe pulse interacts with the Pt and thus an increasing diffraction signal. Our measurements are consistent with observations made in the context of ultra-high frequency sound-wave generation by indirect heating of Ti underneath Cu on a Cu-Ti bilayer, where indirect heating of a Ti layer underneath a Cu layer was shown to generate ultra-high frequency sound-wave packets [43].

To more systematically study the effect of the thickness of the Pt layer on the probe-diffraction decay curves, we fabricated samples in which we kept the Au layer thickness fixed while varying the Pt layer thickness. In Fig. 5(a), we plot the measured front-probe diffraction signal as a function of pump-probe delay from bilayer samples having a buried Pt layer thickness of 0, 2, 5, 15, and 30 nm underneath a 50 nm layer of Au. The pump fluence in these experiments is 0.96 mJ/cm^2. The results clearly show that thicker Pt layers lead to a more rapid decay of the probe diffraction efficiency versus pump-probe time delay. Remarkably, even a Pt layer as thin as 2 nm is capable of speeding up the measured decay significantly.

In Fig. 5(b), we plot the calculated electron temperature at a depth of 8 nm from the top surface of gold as a function of time for these samples. In the simulation, the same parameters were used as in the experiment. The calculations show that the electron temperature decays faster for samples with a thicker layer of platinum buried underneath and are in good agreement with the experimental results. However, the constant level to which the curves decay, seen in the calculation, is somewhat higher compared to what is observed in the experiments.

Optics EXPRESS

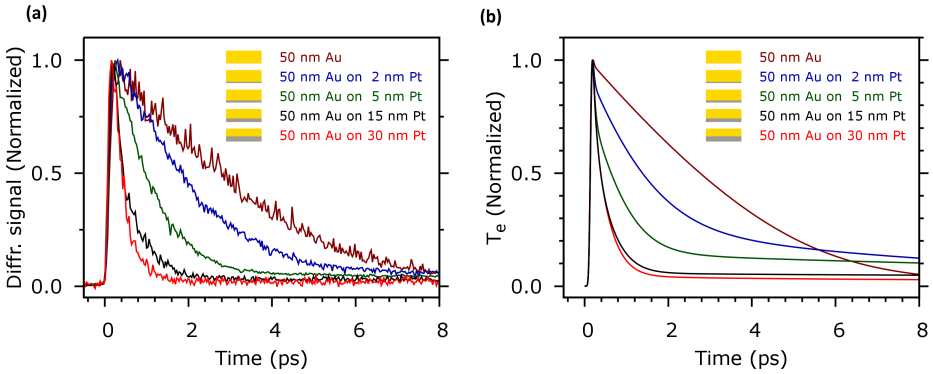

Fig. 5. (a) The measured front-probe diffracted signal vs. pump-probe delay for a pump fluence of 0.96 mJ/cm^2 on bilayer samples with different thicknesses of platinum (0, 2, 5, 15, 30 nm) buried under 50 nm gold, (b) The numerically calculated electron temperature T_e vs. time for these samples using the same pump fluence as used in the experiment.

We can intuitively understand this behavior as a thicker layer of platinum acts as a more effective electron energy heat sink. This results in a higher rate of diffusion of electron energy out of the optical probe interaction region near the Au surface, and a subsequently more rapid drop in electron temperature. This measurement thus shows that some measure of control of the rate of diffusion of electron gas energy between the two metal layers is possible by varying the buried metal thickness. In fact, changing the thickness of the buried platinum also affects the maximum Pt lattice temperature reached, after optical excitation. This study might also help to better understand the ablation mechanism and threshold in metallic bilayers [38].

4.3. Electron dynamics in bilayers with other metals

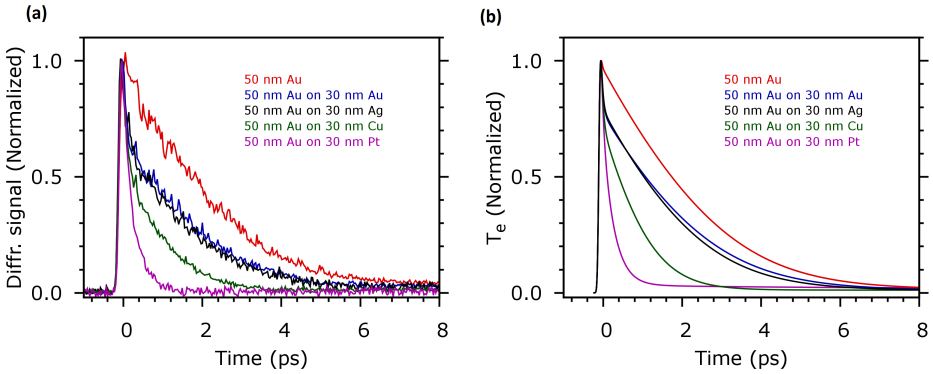

Fig. 6. (a) The measured front-probe diffracted signal vs. time for a pump fluence 0.80 mJ/cm^2 for bilayer samples with different materials buried under 50 nm Au. (b) The numerically calculated electron temperature T_e vs. time for the same pump fluence as used in the experiments.

To confirm that it is the strength of the electron-phonon coupling constant that is responsible for the increase in the observed probe diffraction decay rate, we also fabricated bilayers in which we varied the type of metal underneath the gold layer. In Fig. 6(a) we plot the front-probe diffracted signal as a function of pump-probe time-delay, for bilayers consisting of 50 nm of Au on top of

Optics EXPRESS

30 nm of four different metals, being: Pt, Cu, Ag and Au, (the last case thus consisting of 80 nm of Au in total). For completeness, we also show the results for a 50 nm single layer of gold. The pump fluence in these measurements was 0.80 mJ/cm^2.

The Fig. 6(a) shows that the decay of the diffraction efficiency versus time for 50 nm of Au on Pt, also shown in Fig. 5(a), is the fastest, followed by Au on Cu, which is also faster than 50 nm + 30 nm of Au only, but slower than the signal for Au on Pt. The decay for 50 nm Au on 30 nm Ag is about as fast as that for 50 nm Au + 30 nm Au. In agreement with the results shown in the appendix in Fig. 9, the signal for 80 nm of Au decays faster than the signal for 50 nm of gold.

In Fig. 6(b), we plot the calculated electron temperature at a depth of 8 nm from the surface of Au as a function of time for these samples. The decay of the electron temperature is fastest for the sample with a buried layer of platinum. The decay gets slower as the buried layer is changed from platinum to copper to silver and finally to gold. This is in good agreement with the experimental results. The decay of the measured diffracted signal correlates with the strength of the electron-phonon coupling in the various metals listed in Table 1 (Appendix B), with materials having a stronger electron-phonon coupling showing a faster decay. The electron-phonon coupling constants of Ag and Au are more or less the same and so are the measured decay rates.

4.4. Detection of a buried grating

To demonstrate that thermalized electron gas dynamics can be used to detect buried structures, we evaporated 100 nm Au on a glass substrate and fabricated a 40 nm thick Au grating with a 6 μm pitch and 50% duty cycle with UV lithography on top of this layer, as schematically shown in Fig. 7(a). A similar sample was also made with a 40 nm Cu grating on top of a 100 nm Au layer. We performed a pump-probe experiment with a single pump pulse on these samples by pumping and probing from the *substrate* side. Thus, both the pump and the probe beam see a nominally flat surface and the grating is optically hidden. Since we pump from the glass side, where the gold is flat, we will henceforth refer to the gratings on top as "buried" gratings. We chose to fabricate gratings on top of the flat layer, to ensure that there is no residual topography of the grating at the flat top surface (which, in this case, is at the glass/Au interface). The other way around, evaporating Au onto a metal grating, leaves a residual grating topography at the top surface which gives rise to a significant diffraction, even after polishing. In the experiments described in the previous sections we used two pump pulses, forming a spatially periodic interference pattern, to excite the sample. This gives rise to a spatially periodic electron gas temperature leading to a spatially periodic complex dielectric function. In contrast, here, we use a single pump pulse to homogeneously illuminate the sample. In what follows, we argue that the observation of first-order diffraction in this case is proof that a spatially periodic electron gas temperature pattern is nonetheless also formed. Such an electron gas temperature grating, following homogeneous excitation, can be formed due to the different rates of electron gas energy diffusion above the valleys and above the ridges of the grating. As we have shown in the previous sections (and in the appendix), differences in the electron-energy diffusion rate can be caused both by differences in the thickness of a metal and also by the type of metal buried underneath. The former is illustrated by the gold grating behind a flat gold layer, the latter by a copper grating behind a flat gold layer. In Fig. 7(b), we plot the first-order diffracted signal for both the Au on Au grating and the Cu on Au grating. We find that the onset of diffraction is delayed, in comparison to the measured time-dependent diffraction using two interfering pump-pulses on a flat region on the same sample, by about 0.4 ps. After this time, diffraction is observed but surprisingly, the diffracted signal increases slower than for a single Au layer. For the Au/Au grating the rise time is about 1 ps, whereas for the Cu/Au grating we observe a rise time of about 3 ps. We emphasize that with a single pump, and thus without pump interference grating, the observation of diffraction in itself implies a grating in the optical constants of Au near the glass-Au interface, caused by the buried gratings. Indeed, when we pump the samples in a region where no grating is present and where,

Optics EXPRESS

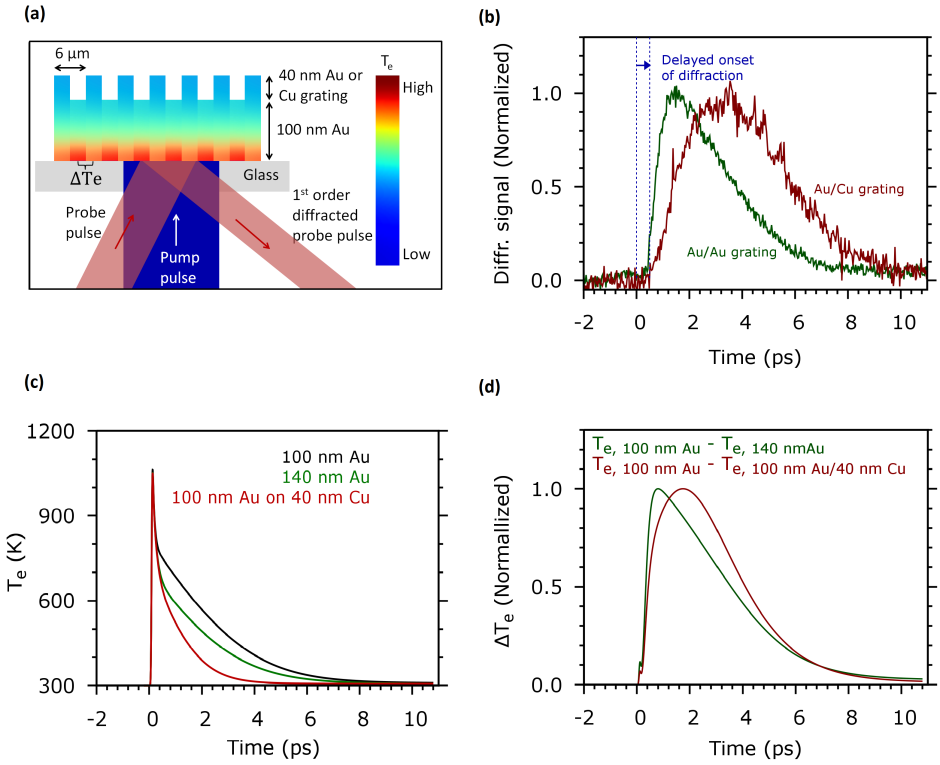

Fig. 7. (a) The schematic of the experimental setup. The single 400 nm pump pulse illuminates the flat 100 nm Au from the glass side. The probe pulse diffracts off the spatially periodic electron temperature that is created due to the difference in the electron diffusion behavior caused by the 40 nm Au/Cu. Schematic of the electron temperature after 1 ps is shown using the colour scheme. (b) The measured diffracted signal vs. time from the glass-Au interface for a pump fluence of 0.80 mJ/cm^2. (c) Numerically calculated electron temperature T_e vs. time for 100 nm Au (black), 140 nm Au (green) and 100 nm Au (red) on 40 nm Cu for a pump fluence of 0.80 mJ/cm^2. (d) The difference between the calculated T_e for 100 nm Au and 140 nm gives the green curve. This is similar to the measured green curve from a 100 nm Au with 40 nm Au grating underneath. The difference between the calculated T_e for 100 nm Au and 140 nm Au/40 nm Cu gives the red curve. This is similar to the measured red curve from a 100 nm Au with 40 nm Cu grating underneath.

for the Au/Au sample, the sample consists of a 100+40 nm single layer of Au, no diffraction was observed. The observation of diffraction also implies that lateral, in-plane diffusion of the electron energy is not strong enough to destroy the grating contrast. This is to be expected considering the large value of 6 μm of the grating period with respect to the typical distance of $\lesssim$ 150 nm over which electron energy can diffuse in gold [44]. We note that in the measurements on flat bilayer samples, shown in Fig. 6, the diffracted signal decays faster for Au on Cu than for Au on Au. The reason for this is that Cu has a larger electron-phonon coupling constant which results in a faster diffusion of electron energy out of the probe interaction region near the gold surface. The diffracted signal dynamics for the Cu/Au grating is slower than for the Au/Au grating. This is in sharp contrast to the faster decay we observe for the Au on Cu flat samples in the diffraction experiments described in section 4.3. To understand this, it is important to realize that here, the grating is also the result of a spatially periodic electron gas temperature $T_e(t)$ giving rise to a spatially periodic dielectric function. In the case of the two-pump-pulse experiments described in

Optics EXPRESS

sections 4.1 to 4.3, the spatially periodic electron gas temperature is the result of excitation of the metal with two spatially and temporally overlapping pump pulses. In contrast, here, using a *single* pump pulse, immediately after optical excitation before energy diffusion has a significant impact on the electron gas temperature, there is no temperature grating. The electron gas temperature is high, but more or less homogeneous along the gold/glass interface. After a short while, electron gas energy diffusion lowers the electron gas temperature at the gold/glass interface, but at a faster rate above the ridges than above the valleys of the buried grating. The resulting temperature contrast (difference) $\Delta T_e(t)$, leads to a grating in the dielectric constant, in a manner similar to the case where two interfering pump pulses were used. There, however, the lowest temperature in the dark fringes is expected to be close to 297 K and the maximum temperature is reached in the bright fringes immediately after optical excitation. Here, for the buried grating, using calculations based on the two-temperature model as shown in Fig. 7(c) and Fig. 7(d), we find that the *difference* temperature shown in Fig. 7(d) reaches its maximum at a time when the absolute electron temperature in the different regions has already dropped significantly as shown in Fig. 7(c). The calculated ΔT_e reaches its maximum value at ≈ 0.8 ps for Au/Au grating whereas the measured diffracted signal reaches its maximum at 1.3 ps. Similarly, for the Cu/Au grating, the calculated ΔT_e reaches a maximum value at 1.8 ps whereas the measured diffracted signal reaches a maximum at 3.6 ps. These calculations contain the essential features of the measurement, in particular the slow rise of the difference temperature, which is more pronounced for the 40 nm Au/100 nm Au sample than for the 40 nm Cu/100 nm Au sample. We note that the decay curves for the electron temperatures, calculated for 100 nm Au, 140 nm Au, and 40 nm Cu on 100 nm Au, are quasi-parallel as shown in Fig. 7(c). This means that small changes in the shape of these signals will have a dramatic effect on the exact time where the difference temperature reaches its maximum.

5. Summary

We have shown pump-probe diffraction measurements of the thermalized electron gas dynamics in single metal layers and in metallic bilayers. Our measurements on Pt/Au samples show a rapid decay in the measured diffracted probe signal, after optical excitation with a pump pulse, indicating a rapid cooling of the electron gas at the gold surface due to the presence of the buried platinum layer. We find that this decay increases with increasing Pt layer thickness. Even for a sample with 5 nm Pt under 150 nm Au, we observe a measurable effect on the shape of the time-dependent diffracted signal as compared to 150 nm Au only, illustrating the sensitivity of electron diffusion near the gold surface on the presence of a buried layer such as Pt. The decay of the diffracted signal is also found to be dependent on the type of buried metal layer and is correlated with the electron-phonon coupling strength of the buried metal. In experiments with a single pump beam, we demonstrate that thermalized electron dynamics can be used for the detection of buried gratings underneath an optically opaque layer of Au. We show that the shape of the time-dependent diffracted signal is different for a Cu grating on Au compared to a Au grating on Au. The peak in the diffracted signal occurs a few picoseconds later compared to what is observed for experiments on non-structured metal layers and bilayers. The TTM numerical calculation of the electron temperatures shows good agreement with our measurements. The experiments demonstrate that thermalized electron gas dynamics can be used to detect optically hidden structures underneath metals like gold and hint at the possibility to image periodic and non-periodic, micro- and nano structures buried below opaque metal layers.

Optics EXPRESS

Appendices

Appendix A: Laser pulse absorption calculation

To calculate the absorption of the light inside the metal layers, we solve Maxwell's equations with the appropriate boundary conditions. This calculation is important in the case of bilayer samples, because the incident laser pulse can directly excite the electrons in the second metal layer. To include the absorption of light in the second layer, we solve Maxwell's equations for a system of four materials as illustrated in Fig. 8. Material 1 and 4 are infinitely thick while materials 2 and 3 have a finite thickness. The first material represents air and material 4 represents glass. Material 2 and material 3 are the Au and Pt metal (or other metals used in the experiment) layers respectively. From the basic electromagnetic equations, we can understand that a wave incident on the interface between material 1 and material 2 will undergo partial reflection into the first material and partial transmission into the second material. The partially transmitted wave undergoes further partial reflection and transmission at the interface between material 2 and 3 and, material 3 and 4 . To calculate the spatial distribution of absorption in material 2 and material 3, we need to obtain the complete electric and magnetic field expressions describing the magnitude and direction of the fields. We assume that all fields propagate perpendicular to the interfaces.

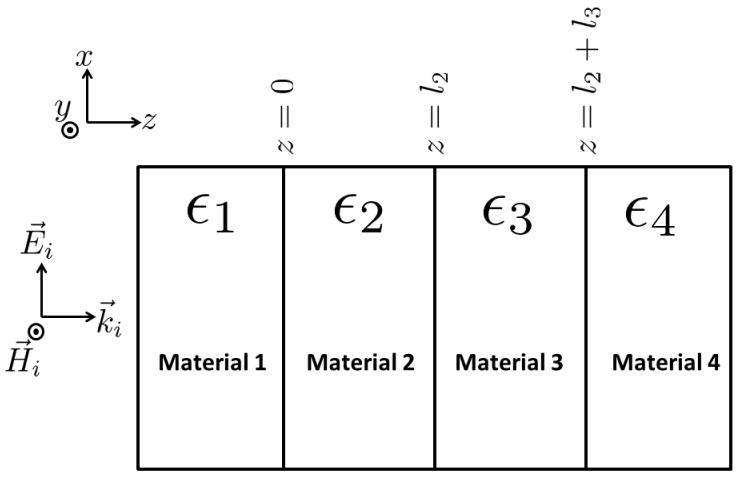

Fig. 8. Geometry used for the calculation: Material 1 and 4 have an infinite extent to the left and right side respectively. Material 2 and 3 have a finite thickness of l_2 and l_3 respectively. The electromagnetic wave originating from material 1 propagates through all four materials after undergoing partial reflection and transmission at each interface.

Due to the non-magnetic nature of gold and platinum we can safely assume $\mu = \mu_0$ for all materials. In absence of any charged particles or currents, we can write the electric and magnetic fields inside each material as

$$\vec{E}(z,t) = E_0(t) \begin{cases} (e^{ik_1 z} + re^{-ik_1 z})\hat{x}, & z < 0 \\ (ae^{ik_2 z} + be^{-ik_2 z})\hat{x}, & 0 < z < l_2 \\ (ce^{ik_3(z-l_2)} + de^{-ik_3(z-l_2)})\hat{x}, & l_2 < z < (l_2 + l_3) \\ t(e^{ik_4(z-(l_2+l_3))})\hat{x}, & z > (l_2 + l_3) \end{cases} \quad (1)$$

Optics EXPRESS

$$\vec{H}(z,t) = \frac{E_0(t)}{\omega\mu}\begin{cases} k_1(e^{ik_1 z} - re^{-ik_1 z})\hat{y}, & z < 0 \\ k_2(ae^{ik_2 z} - be^{-ik_2 z})\hat{y}, & 0 < z < l_2 \\ k_3(ce^{ik_3(z-l_2)} - de^{-ik_3(z-l_2)})\hat{y}, & l_2 < z < (l_2 + l_3) \\ k_4(te^{ik_4(z-(l_2+l_3))})\hat{y}, & z > (l_2 + l_3) \end{cases} \tag{2}$$

where *a, b, c, d, t, r*, k_1 and k_4 are assumed to be real and k_2 = and k_3 are complex. Here $k_2 = \omega\tilde{n}_2/c$ and $k_3 = \omega\tilde{n}_3/c$ with $\tilde{n}_{2,3} = n_{2,3} + i\kappa_{2,3}$ being the complex refractive index of material 2 and 3 respectively. The pulsed excitation is incorporated by our choice of electric field,

$$E_0(z,t) = Ae^{-4ln2(t/\tau_p)^2)} \times e^{(-i\omega t)},$$

where τ_p is the full width at half maximum pulse duration of the electric field envelope and A is the amplitude of the electric field.

We use the boundary condition that both the electric and magnetic field components parallel to the interface are continuous across each interface and solve the resulting set of equations to obtain expressions for *a, b, c, d, t* and *r*. This allows us to write the expression for the space and time-dependent fields in all four materials. From these we calculate the single oscillation time average of the Poynting vector, $\langle\vec{S}\rangle$. From $\langle\vec{S}\rangle$, the optical power absorbed per unit volume is expressed as,

$$\frac{\partial u}{\partial t} = -\vec{\nabla}\cdot\langle\vec{S}\rangle, \tag{3}$$

where u is the electromagnetic energy density. This gives us the information about the distribution of the optical intensity inside all four materials. We use the refractive index n and extinction coefficient κ values of Au and Pt to calculate the optical intensity distribution inside the Au-Pt bilayer [37]. The result is the source term in the two-temperature model.

Appendix B: Two temperature model

The two temperature model is a widely used phenomenological model that describes the electron-lattice dynamics after optical excitation with a laser pulse. In the model, the electron gas is assumed to be thermalized at all times during and after excitation with, and is described by a time-dependent temperature T_e, while the lattice is assumed to have a time-dependent temperature T_l. The time evolution of the temperature is modeled by two coupled differential equations, originally proposed by Anisimov et al. [45] and can, assuming a one-dimensional geometry, be written as [10],

$$C_e(T_e)\frac{\partial T_e}{\partial t} = \frac{\partial}{\partial z}\left(K_e\frac{\partial}{\partial z}T_e\right) - g(T_e - T_l) + \frac{\partial u}{\partial t} \tag{4}$$

$$C_l\frac{\partial T_l}{\partial t} = g(T_e - T_l). \tag{5}$$

Here, C_e and C_l are the respective heat capacities of the electron gas and the lattice, K_e is the thermal conductivity of the electron gas, g is the electron-phonon coupling constant and $\partial u/\partial t$ is the source term. The source term describes when and where energy is deposited in the system by the laser pulse. Note that in Eq. 2, we left out a term for lattice heat diffusion since this is typically slow on the time scales of our experiment. We use the relations $C_e = A_e T_e$ and $K_e = K_0 \times T_e/T_l$ [10] and solve the TTM numerically to calculate the time evolution of T_e and T_l, using the actual experimental parameters and using material properties obtained from literature and shown in Table 1. By assuming instantaneous local thermalization of the electron gas we ignore ballistic transport of the electrons which is known to occur in gold in the first $\approx$ 100 fs [14].

Optics EXPRESS

Table 1. Material constants used in our two temperature model calculations. Listed are the electron-phonon coupling constant g, electron specific heat constant A_e, thermal conductivity K_0 at $T = 273$ K and lattice heat capacity C_l. [10, 46–48]. We have used the relations $C_e = A_e T_e$ and $K_e = K_0 \times T_e/T_l$ [10].

Metals	g (10^{16} $Wm^{-3}K^{-1}$)	A_e ($Jm^{-3}K^{-2}$)	K_0 ($Wm^{-1}K^{-1}$)	C_l (10^5 $Jm^{-3}K^{-1}$)
Gold	1.6	71	318	24.3
Platinum	100	740	73	27.0
Copper	8.0	98	401	35.0
Silver	1.9	63	428	25.0

Appendix C: Dependence of electron dynamics on Au layer thickness

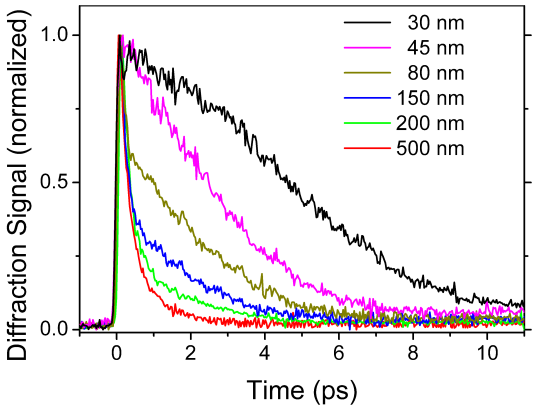

Fig. 9. Diffracted front-probe signal vs. pump-probe delay for different gold thicknesses at a pump fluence of 0.8 mJ/cm^2.

In Fig. 9, the normalized first-order diffracted signal is plotted as a function of pump-probe delay for different thicknesses of the gold layer. At delay zero, when pump and probe pulses overlap in time, the diffraction efficiency rises to its maximum value within less than 100 fs. For gold layers thicker than about 100 nm, this is followed by a rapid decrease of the diffraction efficiency to zero within a few ps. In contrast, for thin gold layers, the decrease of the diffraction efficiency proceeds at a much slower pace lasting up to 10 ps for the 30 nm sample. For thin layers, after 0.5 ps, the diffraction efficiency appears to decay linearly with delay for a few picoseconds. The results are similar to those obtained by Hohlfeld et al. who measured the transient reflectivity of gold layers [14] after illumination with 400 nm pulses, although there are some subtle differences between their results and ours. Most notably, the fast and sharp peak around delay zero with a width of about 0.5 ps, visible in our measurements in all but the 30 and 45 nm thick samples, is absent in the Hohlfeld paper. We think that this is due to the relatively long pulses of 200 fs used in their experiments, as this would partially smear out rapidly changing signals. The initial fast decay observed for the thicker gold layers is caused by rapid electron energy diffusion out of the tens of nanometer thick surface layer probed by the 800 nm probe pulse. For thin layers, the electron energy becomes relatively homogeneously distributed over the entire thickness of

Optics EXPRESS

the metal layer almost immediately, such that net spatial diffusion of energy out of the probe optical interaction region near the surface becomes negligible. The diffraction signal decay is then dominated by cooling of the electron gas by transfer of electron energy to the lattice, a process that is relatively slow for Au [14].